Supporting Information

Cideciyan et al. 10.1073/pnas.1218933110

SI Materials and Methods

Human Subjects. ***Retinal cross-sectional imaging and analysis.*** Optical coherence tomography (OCT) scans were obtained with a spectral domain (SD) system (RTVue-100; Optovue). The Line or HD-Line protocols were used to obtain 4.5- or 9-mm-long overlapping scans along vertical meridian crossing the fovea and extending up to 9-mm eccentricity (1, 2). Postacquisition processing of data was performed with custom programs (MatLab 7.5; MathWorks). OCT scans were aligned by the major retinal pigment epithelium (RPE) reflection in each longitudinal reflectivity profile (LRP), registered, merged, and resampled at 512 LRPs per 4.5 mm. Outer photoreceptor nuclear layer (ONL) was segmented manually using a combination of intensity and local slope information of LRPs (2, 3). Specifically, the hyporeflective layer corresponding to the ONL (and the Henle fiber layer) was detected by placing the boundaries at the minimum LRP slope immediately distal (sclerad) to the hyperreflective outer plexiform layer (OPL) and maximum LRP slope proximal (vitread) to the hyperreflective outer limiting membrane (OLM) layer. The ONL was usually first defined in centrally retained regions and extended laterally to more peripheral regions with thinner ONL. Some data from the earliest visit in a subset of patients were acquired on a time-domain system (OCT3; Carl Zeiss Meditec) and analyzed as previously described (4–6).

Because normal ONL thickness changes with eccentricity, a parameter named ONL fraction was derived by dividing ONL thickness measured at each location by the mean normal ONL thickness at the corresponding retinal location (7). ONL fraction values were averaged across 1.2-mm spans between 1.2- and 8.4-mm superior retina and 1.2- and 6-mm inferior retina to reduce noise. A model of disease progression consisting of a delayed exponential function was hypothesized to underlie the change of ONL fraction with age (2, 8). Serial data were obtained in patients in yearly (or longer) intervals, and the rates of exponential decay associated with each pair of sequential data were calculated. The median value of all of the progression rates was assumed to estimate, to a first approximation, the underlying invariant progression rate. Next, the onset of the photoreceptor degeneration was estimated by fitting (least squares on log-linear coordinates) the invariant rate to all data from each individual retinal location and calculating the age at which the function intercepts the unity ONL fraction. The overall variation expected along the natural history of photoreceptor degeneration across all untreated control eyes and all retinal locations was estimated as the 2 SD of the residuals between the data replotted as a function of time after the onset of degeneration and the underlying natural history model (Fig. 1*F*). Serial data from study eyes (both treated and untreated retinal locations) of *RPE65*-LCA were similarly processed to derive ONL fraction. Next, data from each retinal location were horizontally shifted to match the baseline values to the natural history of progression, and the posttreatment values were compared with the expected natural history of degeneration (Fig. 2*B*).

Psychophysical studies. Visual sensitivity of patients was determined with a modified computerized perimeter (Humphrey Field Analyzer; Zeiss) as published (7, 9). The achromatic (white) stimulus was 1.7° in diameter and 200 ms in duration (maximum luminance = 3,180 cd.m^{-2}), and it was presented after patients' eyes were adapted to darkness for an extended (3–8 h) period (7). Tested loci were along the vertical meridian crossing fixation. In all patients, testing was performed in study and control eyes at baseline and posttreatment time points. In a subset of patients, there was additional data available ranging up to 4.5 y before treatment, providing serial measurements for up to 6.7 y. Retinal loci were sampled at 0.6-mm intervals up to 9-mm eccentricity from the fixation. Loci were tested using a red fixation target with a variable intensity that was adjusted to be visible for each subject.

The dynamic range of the native instrument (normally 5 $\log_{10}$ units) was shifted with the use of neutral density filters (up to 3 $\log_{10}$ units) to circumvent ceiling effects that would be otherwise expected in normal subjects and treated regions of some of the patients. In treated eyes, multiple tests were performed with overlapping dynamic ranges; floor or ceiling values were discarded, and best sensitivities were used.

Dogs. ***Retinal cross-sectional imaging and analysis.*** *En face* and retinal cross-sectional imaging was performed with the dogs under general anesthesia (10, 11). Overlapping *en face* images of reflectivity with near-infrared (NIR) illumination (820 nm) were obtained (Spectralis) with 30°- and 55°-diameter lenses to delineate fundus features, such as optic nerve, retinal blood vessels, boundaries of injection blebs, retinotomy sites, and other local changes. Custom programs (MatLab 7.5; MathWorks) were used to digitally stitch individual photos into a retina-wide panorama. In a subset of eyes, short-wavelength (488 nm) illumination was used to delineate the boundary of the tapetum and pigmented RPE. SD-OCT was performed with linear and raster scans (RTVue-100 by Optovue or Spectralis HRA+OCT). Linear scans were placed across regions or features of interest, such as bleb boundaries, to obtain highly resolved local retinal structure. The bulk of the cross-sectional retinal information was obtained from overlapping raster scans (6 × 6 mm, 101 lines of 513 LRPs each, no averaging; Optovue; 9 × 6 mm, 49 lines of 1,536 LRPs each, averaging 8–10; Spectralis) covering large regions of the retina extending ~24 × 24 mm^2.

Postacquisition processing of OCT data was performed with custom programs (MatLab 7.5; MathWorks). For retina-wide topographic analysis, integrated backscatter intensity (OCT projection image) of each raster scan was used to locate its precise location and orientation relative to retinal features visible on the retina-wide mosaic formed by NIR reflectance images. Individual LRPs forming all registered raster scans were allotted to regularly spaced bins (1° × 1°) in a rectangular coordinate system centered at the optic nerve; LRPs in each bin were aligned and averaged. Intraretinal peaks and boundaries corresponding to histologically definable layers were segmented semiautomatically with manual override using both intensity and slope information of backscatter signal along each LRP. Specifically, the retina–vitreous interface, OPL, OLM, signal peak near the inner/outer segment junction, and RPE were defined. In the superior retina of the dog, backscatter from the tapetum forms the highest intensity peak, and RPE and inner/outer segment peaks are located vitreal to the tapetal peak. ONL thickness was defined from the sclerad transition of the OPL to the OLM, and ONL thickness topography was calculated. For all topographic results, locations of blood vessels, optic nerve head, and bleb boundaries were overlaid for reference.

Normal ONL maps were registered by the locus of the optic nerve head and rotated to bring the superior central vessels in congruence. A map of mean normal ONL thickness was derived. *RPE65*-mutant dog ONL maps similarly were registered to the normal map, and an ONL fraction was derived by dividing each thickness by the corresponding mean normal value. This derived ONL fraction map was sampled at five locations: two loci were in

the superior retina, two loci were in the inferior retina, and one locus was in the central nasal retina near the visual streak (Fig. 3 *A*–*C*). Natural history of photoreceptor degeneration was estimated by plotting ONL fraction values at these loci against age.

Electroretinography. Dogs were dark-adapted overnight, premedicated, and anesthetized as described (12–15). Pupils were dilated. Pulse rate, oxygen saturation, and temperature were monitored. Full-field electroretinograms (ERGs) were recorded with Burian–Allen (Hansen) contact lens electrodes and one of two different computer-based systems with similar flash stimuli. Dogs 23–27 (D23–D27) were tested with the EPIC-XL (LKC Technologies) equipment previously described (15). D16, D17, D19, and D22 were tested with an Espion (Diagnosys LLC) system. White flashes (0.4–1.2 log scot-cd.s.m^{-2}) were presented under dark-adapted conditions or flickered at 29 Hz on a rod-desensitizing background (0.8 log cd.m^{-2}). In some case, high-energy flashes were used to evoke photoresponses.

Morphological evaluation. Assessment of photoreceptor structure was made in 6- to 7-μm-thick retinal sections stained with H&E from eyes that were fixed in Bouin or Excalibur solution as previously described (16, 17). Using the *en face* retinal images and ONL topography maps as guides, eyes were trimmed to section through the treated and untreated regions. To correlate the degree of structural preservation with RPE65 expression, immunolabeling of adjacent sections was done with and without antigen retrieval using a polyclonal anti-RPE65 antibody (RPE65 PETLET; a gift from T. M. Redmond, Laboratory of Retinal Cell and Molecular Biology, National Eye Institute, National Institutes of Health, Bethesda) combined, when appropriate, with monoclonal antirhodopsin antibody (MAB5316; Millipore) using methods previously described (17). As control, we used retinal sections processed in the same manner from dogs that were WT or homozygous mutants at the RPE65 locus.

1. Cideciyan AV, et al. (2011) Cone photoreceptors are the main targets for gene therapy of NPHP5 (IQCB1) or NPHP6 (CEP290) blindness: Generation of an all-cone Nphp6 hypomorph mouse that mimics the human retinal ciliopathy. *Hum Mol Genet* 20(7):1411–1423.
2. Jacobson SG, et al. (2011) Retinal disease course in Usher syndrome 1B due to MYO7A mutations. *Invest Ophthalmol Vis Sci* 52(11):7924–7936.
3. Jacobson SG, et al. (2008) Photoreceptor layer topography in children with leber congenital amaurosis caused by RPE65 mutations. *Invest Ophthalmol Vis Sci* 49(10):4573–4577.
4. Huang Y, et al. (1998) Relation of optical coherence tomography to microanatomy in normal and rd chickens. *Invest Ophthalmol Vis Sci* 39(12):2405–2416.
5. Jacobson SG, et al. (2005) Identifying photoreceptors in blind eyes caused by *RPE65* mutations: Prerequisite for human gene therapy success. *Proc Natl Acad Sci USA* 102(17):6177–6182.
6. Jacobson SG, et al. (2007) Human cone photoreceptor dependence on RPE65 isomerase. *Proc Natl Acad Sci USA* 104(38):15123–15128.
7. Cideciyan AV, et al. (2008) Human gene therapy for RPE65 isomerase deficiency activates the retinoid cycle of vision but with slow rod kinetics. *Proc Natl Acad Sci USA* 105(39):15112–15117.
8. Cideciyan AV, et al. (2009) ABCA4 disease progression and a proposed strategy for gene therapy. *Hum Mol Genet* 18(5):931–941.
9. Jacobson SG, et al. (1986) Automated light- and dark-adapted perimetry for evaluating retinitis pigmentosa. *Ophthalmology* 93(12):1604–1611.
10. Cideciyan AV, et al. (2005) In vivo dynamics of retinal injury and repair in the rhodopsin mutant dog model of human retinitis pigmentosa. *Proc Natl Acad Sci USA* 102(14):5233–5238.
11. Beltran WA, et al. (2012) Gene therapy rescues photoreceptor blindness in dogs and paves the way for treating human X-linked retinitis pigmentosa. *Proc Natl Acad Sci USA* 109(6):2132–2137.
12. Acland GM, Aguirre GD (1987) Retinal degenerations in the dog: IV. Early retinal degeneration (erd) in Norwegian elkhounds. *Exp Eye Res* 44(4):491–521.
13. Aguirre GD, Acland GM (1988) Variation in retinal degeneration phenotype inherited at the prcd locus. *Exp Eye Res* 46(5):663–687.
14. Acland GM, et al. (2001) Gene therapy restores vision in a canine model of childhood blindness. *Nat Genet* 28(1):92–95.
15. Acland GM, et al. (2005) Long-term restoration of rod and cone vision by single dose rAAV-mediated gene transfer to the retina in a canine model of childhood blindness. *Mol Ther* 12(6):1072–1082.
16. Jacobson SG, et al. (2006) Safety of recombinant adeno-associated virus type 2-RPE65 vector delivered by ocular subretinal injection. *Mol Ther* 13(6):1074–1084.
17. Kuznetsova TS, et al. (2012) Exclusion of RPGRIP1 ins44 from primary causal association with early-onset cone-rod dystrophy in dogs. *Invest Ophthalmol Vis Sci* 53(9):5486–5501.

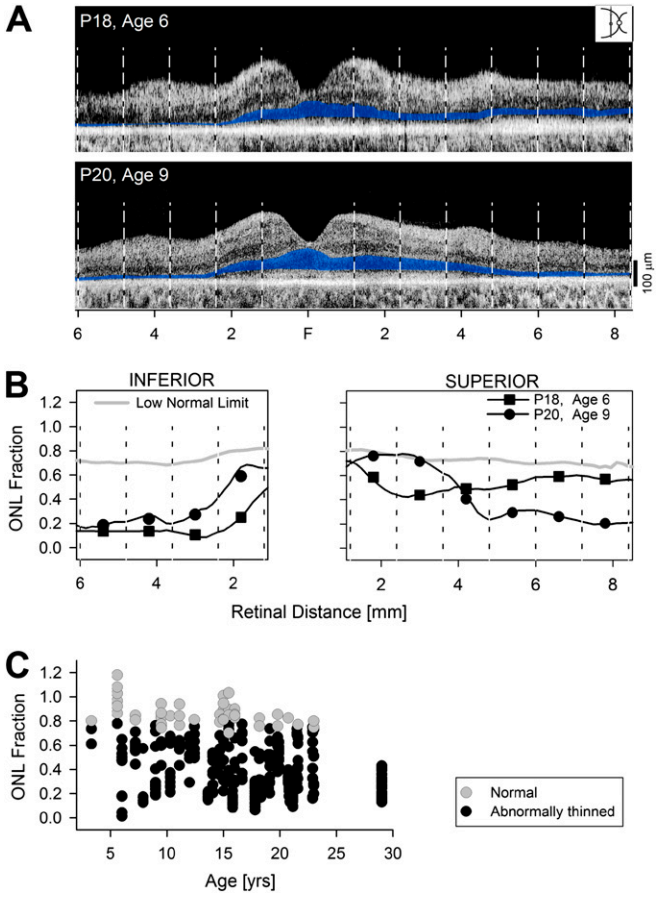

Fig. S1. ONL thickness in patients with *RPE65*-LCA at different ages. (*A*) Cross-sectional retinal images along the vertical meridian crossing the fovea (schematic in *Inset*) in two young patients, patient 18 (P18) and P20, at ages 6 and 9 y, respectively. ONL thickness is colored blue on images. Superior retina is to the right. Vertical dashed lines delimit the 10 retinal regions analyzed in each eye. (*B*) ONL fraction (of mean normal value) of the two patients shown in *A* plotted as function of eccentricity. ONL fraction of unity represents the mean normal at each location, and lower limit (mean − 2 SD) of normal is shown with the gray line. ONL fraction is abnormally thin at all locations in both patients. (*C*) ONL fraction measured along the vertical meridian in patients with *RPE65*-LCA and plotted as a function of age. In *B* and *C*, black symbols represent abnormally thinned loci, and gray symbols represent loci with normal thickness.

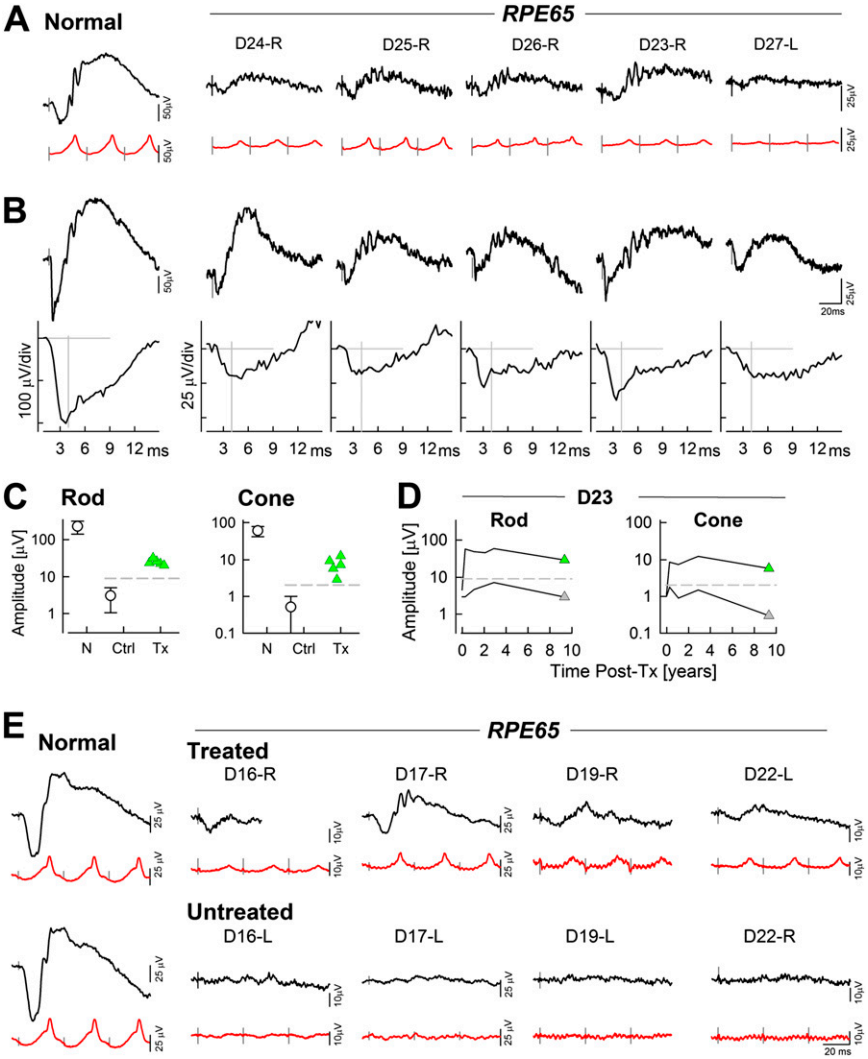

Fig. S2. Restoration of rod and cone retinal function after a single subretinal gene therapy treatment in *RPE65*-mutant dogs treated early and evaluated up to a decade later (*A*–*D*) and treated late and evaluated 1 mo after the treatment (*E*) compared with normal. (*A*) ERGs evoked by standard white flashes presented under dark-adapted (DA) (black traces) or light-adapted (LA) (red traces) conditions. Black vertical lines show the timing of the flashes. (*B*) ERG photoresponses evoked by white flashes of high energy under dark-adapted conditions; same data are shown on slow (*Upper*) and fast (*Lower*) time scales to allow interpretation of late and early components, respectively. Gray lines show the baseline and the 4-ms time point where rod photoreceptor responses were measured. (*C*) Comparison of rod and cone function in the treated *RPE65*-mutant dogs (Tx; green triangles) compared with previously published (15) normal (N) and untreated control (Ctrl) eyes. Rod function shown refers to the DA ERG photoresponse amplitude at 4 ms, and cone function refers to the peak amplitude of the LA 29-Hz waveform. Horizontal dashed lines represent the upper limit (mean + 3 SD) of the respective measurement in the group of control eyes. (*D*) Durability of the rod and cone ERG amplitudes in D23 treated a decade earlier. Subretinally treated right eye is shown with green symbols, and the intravitreally treated left eye is shown with gray symbols. Lines show previously published data extending to age of 3 y (15). Slight reduction of the ERG amplitudes between ages 3 and 10 y is expected from aging effects (12, 13). (*E*) Bilateral ERGs recorded with similar methods and stimuli as shown in *A* in a normal dog and four unilaterally treated *RPE65*-mutant dogs. Treatments were applied at late ages ranging from 4.9 to 6.6 y. ERG recordings performed 1 mo later show definite treatment effects in the eyes with gene therapy.

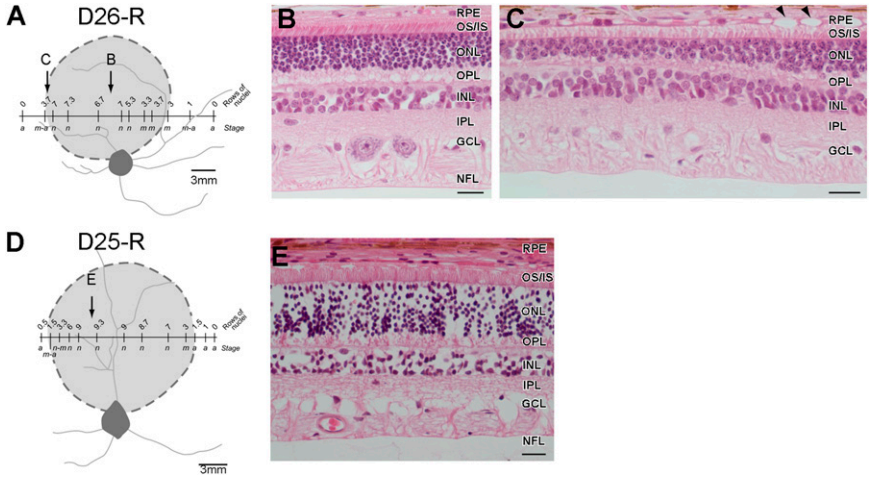

Fig. S3. Gene augmentation therapy at 1.9 y in right eyes of D26 and D25 rescues photoreceptors in the canine LCA. (*A* and *D*) Schematic representation of the *en face* images showing the treatment areas when imaged at 6.7 y of age (dashed lines), on which is superimposed the ONL counts (mean of three values in area sampled) and disease staging (*a*, advanced atrophy with gliosis and loss of retinal layer organization; *m*, moderate photoreceptor loss with 1/3 to 1/2 of ONL remaining; *n*, normal) assessed at 6.9 (D26) and 8.2 (D25) y of age. (*B*, *C*, and *E*) Representative photomicrographs taken from areas identified in *A* and *D*. In the treatment area, there is normal retinal preservation (*B* and *E*). At the edge of the treatment border (*C*), the photoreceptor layer becomes attenuated. GCL, ganglion cell layer; INL, inner nuclear layer; NFL, nerve fiber layer; OS/IS, outer and inner segment layer. (Calibration marker: 20 μm.)

Table S1. Untreated control eyes of *RPE65*-LCA patients

			Retinal structure and visual function	
Patient*	Eye	Mutation	Age at first visit (y)	Follow-up (y)
P1	R	E417Q/E417Q	21	5.5
P2	L	R44Q/R91W	19	6.7
P3	L	Y368H/Y368H	19, 20[†]	6.3, 4.9[†]
P4	L	G40S/H182Y	29	4.2
P5	R	R97del20bp/R97del20bp	17	6.0
P6	R	L341S/L341S	20	4.8
P7	R	IVS1+1G > T/IVS1+1G > T	15	3.4
P8	R	V287F/V287F	13	4.9
P9	R	IVS2-2A > T/L341S	10	3.8
P11	L	V353ins1bp/R91W	23	6.6
P12	L	IVS2-2A > T/L341S	12	4.3
P13	R	R91W/R91W	7	5.1
P14	L	IVS1+5G > A/Y239D	16	1.9
P15	L	Y368H/K354ins1bp	18	1.2
P16	R	R91W/R91W	3	—
P17	R, L	A500del5bp/A500del5bp	5, 9[‡]	—
P18	L	R44Q/R44Q	6	—
P19	L	R44Q/R44Q	7	—
P20	R	A500del5bp/A500del5bp	9	—
P21	L	L408P/L408P	12	—
P22	R	R91Q/R91W	14	—
P23	R, L	G40S/R91Q	19	5.8

L, left eye; R, right eye.

*P1–P15 refer to the untreated eyes of patients taking part in the clinical trial of gene augmentation therapy in the contralateral eye [same nomenclature as used in the work by Jacobson et al. (1)]; P16–P23 refer to patients who have not been treated in either eye. P10 was not included, because severe keratconus and nystagmus in the untreated left eye precluded high-quality imaging. P9 and P12, P13 and P16, P17 and P20, and P18 and P19 are sibling pairs.

[†]Visual function was available for a visit earlier than retinal structure.

[‡]Two eyes were scanned at different visits.

1. Jacobson SG, et al. (2012) Gene therapy for leber congenital amaurosis caused by *RPE65* mutations: Safety and efficacy in 15 children and adults followed up to 3 years. *Arch Ophthalmol* 130(1):9–24.

Table S2. Gene therapy-treated study eyes of *RPE65*-LCA patients

Patient*	Eye	Age at treatment (y)	Retinal structure and visual function follow-up (y)
P1	L	24	2.3
P2	R	23	3.2
P4	R	30	3.1
P6	L	22	3.1
P7	L	15	3.1
P8	L	16	2.2
P9	L	11	2.1
P11	R	27	2.0
P13	L	11	1.0
P14	R	17	1.4
P15	R	18	1.2

*Same nomenclature as used in the work by Jacobson et al. (1) for P1–P15 taking part in the clinical trial of gene therapy. P3, P5, P10, and P12 are not included, because they did not have either a treatment region crossing the vertical meridian or a reliable visual improvement corresponding to the vertical meridian analyzed.

1. Jacobson SG, et al. (2012) Gene therapy for leber congenital amaurosis caused by *RPE65* mutations: Safety and efficacy in 15 children and adults followed up to 3 years. *Arch Ophthalmol* 130(1):9–24.

Table S3. Eyes of *RPE65*-mutant and normal dogs and ages (y) when evaluations were performed

Dog	Eye	Tx	OCT	ERG	Histology
Normal					
D1	R	—	0.1	—	—
D2	R	—	0.3	—	—
D3	R, L	—	0.4	—	—
D4	R	—	—	—	0.6
D5	R	—	—	—	0.6
D6	R	—	0.8	—	—
D7	L	—	2.7	—	—
D8	L	—	3.8	—	—
D9*	L	—	7.4	—	—
D10	R	—	—	—	7.8
D11*	R, L	—	8.0	—	—
RPE65-mutant					
Natural history (no Tx)					
D12	R	—	—	—	1.3
D13	R, L	—	—	—	1.4
D14	L	—	—	—	1.4
D15	L	—	—	—	1.4
D16	L	—	4.8	—	—
D17	L	—	4.8	—	—
D18	L	—	5.0	—	—
D19	L	—	5.1	—	—
D20	R, L	—	5.2	—	—
D21	R, L	—	5.2	—	—
D22	R	—	6.4	—	—
D23	L	—†	9.7	9.7	—
Tx at dysfunction stage/evaluation at dysfunction and degeneration stage					
D24	R	1.8	6.6	6.6	8.1
D25	R	1.9	6.7	6.7	8.2
D26	R	1.9	6.7	6.7	6.9
D27	L	2.4	7.2	7.2	7.2
D23	R	0.3	9.7	9.7	11.2
Tx at dysfunction and degeneration stage/evaluation at dysfunction and degeneration stage					
D16	R	4.9	5.9	5.0	—
D17	R	4.9	5.9	5.0	—
D19	R	5.3	6.3	5.4	—
D22	L	6.6	7.9	6.7	—

L, left eye; R, right eye; —, not performed.
*D9 and D11 are heterozygous carriers of the *RPE65* mutation.
†D23 L was injected intravitreally and is considered effectively as untreated (1, 2).

1. Acland GM, et al. (2001) Gene therapy restores vision in a canine model of childhood blindness. *Nat Genet* 28(1):92–95.
2. Acland GM, et al. (2005) Long-term restoration of rod and cone vision by single dose rAAV-mediated gene transfer to the retina in a canine model of childhood blindness. *Mol Ther* 12(6):1072–1082.